JOC The Journal of Organic Chemistry

Article

pubs.acs.org/joc

Photoactivatable Anthracenes

Ek Raj Thapaliya, Burjor Captain, and Françisco M. Raymo*

Laboratory for Molecular Photonics, Department of Chemistry, University of Miami, 1301 Memorial Drive, Coral Gables, Florida 33146-0431, United States

Supporting Information

ABSTRACT: Fifteen substituted maleimide cycloadducts of anthracene derivatives were synthesized in one or two steps from available precursors in yields ranging from 32 to 63%. They differ in the nature of the group on the maleimide nitrogen atom and of the substituents on the anthracene platform. In all instances, the introduction of a maleimide bridge across positions 9 and 10 of the anthracene skeleton isolates electronically its peripheral phenylene rings and suppresses its characteristic fluorescence. The cycloadducts with a 4-(dimethylamino)phenyl group on the maleimide nitrogen atom undergo retro-cycloaddition upon ultraviolet illumination with quantum yields ranging from 0.001 to 0.01. This structural transformation restores the aromatic character of the central ring of the oligoacene chromophore and activates its emission with fluorescence quantum yields ranging from 0.07 to 0.85. Thus, this particular choice of building blocks for the construction of photoresponsive compounds can translate into viable operating principles for fluorescence activation and, ultimately, lead to the realization of valuable photoactivatable fluorophores for imaging applications.

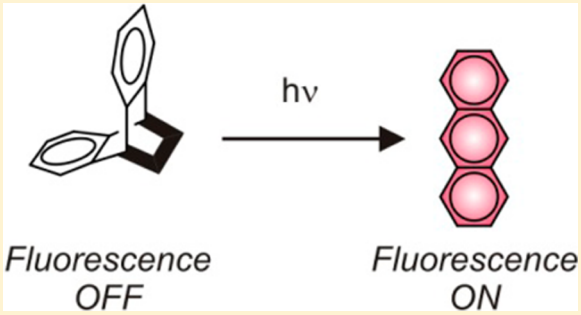

INTRODUCTION

The photochemical conversion of a nonemissive reactant into an emissive product offers the opportunity to activate fluorescence under the influence of optical stimulations.[1−6] Specifically, a pair of independent irradiation sources, operating at distinct wavelengths, can excite reactant and product respectively to induce the photochemical transformation of the former and the emission of the latter. Under these conditions, the spatial overlap of the two illuminating beams and their temporal interplay permits the activation of fluorescence exclusively within a defined region of space at a given interval of time. In turn, the sequential acquisition of fluorescence images, after a single activation event, enables the monitoring of the translocation of the activated emitters in real time.[7−12] Alternatively, the sequential localization of emitters, activated at distinct intervals of time, with single-molecule precision allows the reconstruction of images with spatial resolution at the nanometer level.[13−18] These ingenious imaging schemes provide the possibility to track dynamic events and visualize nanoscaled features respectively in a diversity of specimens and, therefore, are becoming particularly valuable in biological and materials sciences. Nonetheless, their practical implementation is simply impossible with conventional fluorophores and, instead, strictly demands the unique combination of photochemical and photophysical properties associated with their photoactivatable counterparts. Thus, the identification of viable structural designs to photoactivate fluorescence is essential to foster the further development of such promising analytical techniques.

The anthracene skeleton is a convenient building block for the construction of photoactivatable fluorophores. In fact, early examples of fluorescence photoactivation were designed around the structural and spectroscopic properties of this particular chromophore.[19,20] These seminal studies were aimed at the development of photosensitive materials for photographic applications and relied on the introduction of a photocleavable anhydride bridge across positions 9 and 10 of the anthracene platform. This particular bridging unit was designed to isolate electronically the two peripheral phenylene rings of the oligoacene skeleton and suppress its characteristic fluorescence. Upon ultraviolet illumination, the anhydride bridge cleaves into a molecule of carbon dioxide and one of carbon monoxide to restore the aromatic character of the central benzene ring together with the emission of the regenerated anthracene fluorophore. Similarly, two carbon atoms within one of the multiple rings on an oligoacene chromophore can also be connected through an α-diketone bridge to interrupt electronic delocalization across the aromatic platform.[21−25] This particular functional group cleaves into two molecules of carbon monoxide upon excitation to restore the parent oligoacene and its spectroscopic signature. In fact, these operating principles have also been exploited to activate the fluorescence of a few anthracene derivatives.[24h,i,25]

As an alternative to the introduction of photocleavable carbonyl groups, the cycloaddition of appropriate dienophiles to the central ring of anthracene derivatives can also isolate

Received: February 24, 2014
Published: April 9, 2014

dx.doi.org/10.1021/jo5004482 | J. Org. Chem. 2014, 79, 3973−3981

electronically the peripheral phenylene rings with photoresponsive bridges.[26−29] Specifically, a handful of alkenes and a few acylnitroso compounds form photolabile cycloadducts capable of undergoing retro-cycloadditions under illumination to restore the aromatic character of the oligoacene platform. The synthetic accessibility of these particular cycloadducts, together with the opportunity to regulate the spectroscopic signature of the anthracene chromophore with the manipulation of its substituents, can translate into the realization of versatile photoactivatable fluorophores. Nonetheless, the potential of these photochemical transformations to activate fluorescence remains essentially unexplored. These considerations suggest the possibility of assembling a series of anthracene cycloadducts differing in their substituents with the ultimate goal of identifying an optimal structural design for fluorescence photoactivation. Indeed, this paper reports the synthesis of a family of *N*-arylmaleimide cycloadducts, their structural characterization, as well as the investigation of their photochemical and photophysical properties.

RESULTS AND DISCUSSION

Synthesis and Structural Characterization. The cycloaddition of maleic anhydride on the central ring of anthracene introduces a bridge between positions 9 and 10 of the oligoacene platform in the shape of cycloadduct **1** (Figure 1).[30]

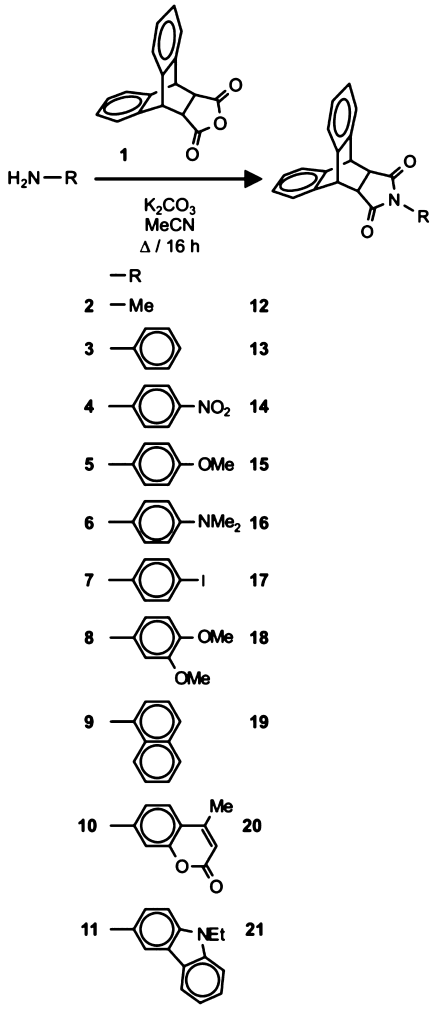

Figure 1. Synthesis of **12**−**21**.

This compound is a valuable precursor for the generation of an entire family of anthracene cycloadducts, differing in the nature of the bridging unit. Specifically, treatment of **1** with primary amines **2**−**11**, in the presence of potassium carbonate, produces imides **12**−**21** in yields ranging from 32 to 63%.[31]

In addition to varying the group on the maleimide bridge, substituents can be introduced on either the two *o*-phenylene rings or positions 9 and 10 of these anthracene cycloadducts. Specifically, the cycloaddition of maleimide **22** (Figure 2) on

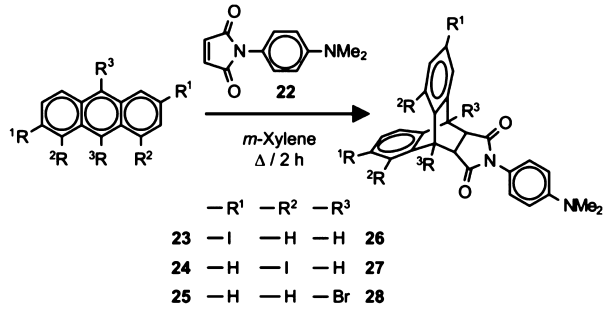

Figure 2. Synthesis of **26**−**28**.

the central ring of substituted anthracenes **23**−**25** generates adducts **26**−**28** in yields ranging from 36 to 55%. Alternatively, reaction of maleic anhydride (**29** in Figure 3) with substituted anthracenes **30** and **31** produces anhydrides **32** and **33**, respectively.[31] Treatment of these compounds with **6**, in the presence of potassium carbonate, produces **34** and **35** in yields of 55 and 45% respectively.

The structural identity of all compounds was confirmed by electrospray ionization mass spectrometry as well as ^{1}H and ^{13}C nuclear magnetic resonance (NMR) spectroscopies (Figures S1−S12, Supporting Information). In addition, single crystals suitable for X-ray diffraction analysis were obtained for **15**, **16**, **18**−**21**, **28**, **34**, and **35**. The resulting structures (Figure 4 and Tables S1−S3, Supporting Information) clearly reveal the maleimide bridge across positions 9 and 10 of the anthracene platform in all instances. The sp^3 hybridization of the two bridgehead carbon atoms forces the peripheral *o*-phenylene rings out of planarity and interrupts electronic delocalization, in agreement with the rationale behind the design of these compounds.

Photochemical and Photophysical Properties. The absorption spectrum of anthracene (**36** in Figure 5) in acetonitrile shows the characteristic vibronic structure of this oligoacene chromophore between 300 and 390 nm (Figure 5, a). Excitation within this range of wavelengths results in intense fluorescence (Figure 5, b). The introduction of a maleimide bridge across positions 9 and 10 isolates electronically the two peripheral phenylene rings, alters drastically the absorption spectrum and suppresses fluorescence. For example, the absorption and emission spectra (Figure 5, c and d) of adduct **12** do not reveal any bands at wavelengths longer than 300 nm, under otherwise identical experimental conditions.

Ultraviolet illumination (254 nm, 0.4 mW cm^{-2}) of adducts **12**−**21** in acetonitrile results in noticeable absorption and emission changes only for **16** and **17**. Specifically, comparison of the absorption and emission spectra recorded before (Figure 6, a and b) to those measured after (Figure 6, c and d) irradiation of **16** reveals the appearance of the characteristic anthracene bands. Indeed, retro-cycloaddition of **16** occurs upon excitation to form **22** and **36**. A plot of the absorbance

dx.doi.org/10.1021/jo5004482 | J. Org. Chem. 2014, 79, 3973−3981

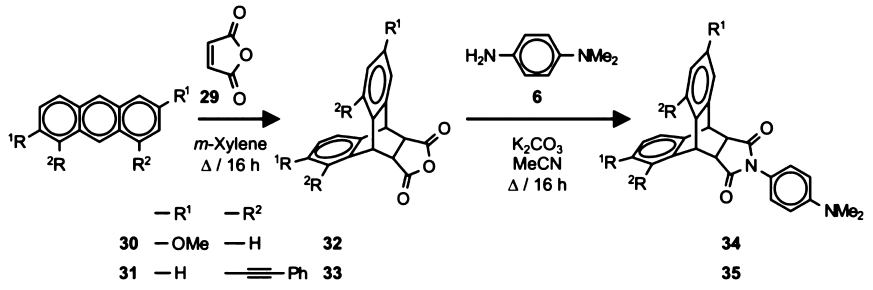

Figure 3. Synthesis of **34** and **35**.

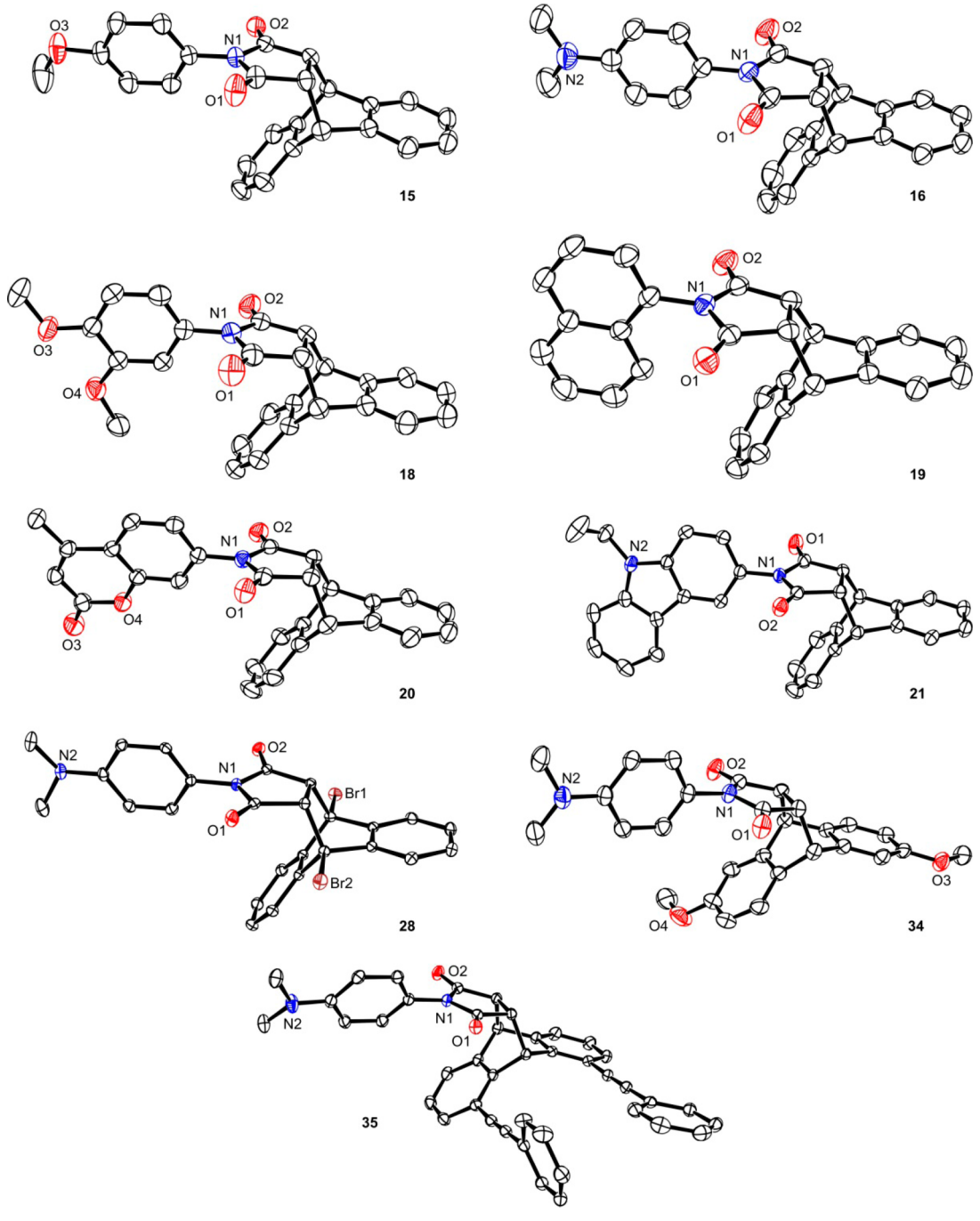

Figure 4. ORTEP representations of the geometries adopted by **15**, **16**, **18**–**21**, **28**, **34**, and **35** in single crystals, showing 30% (**15**, **34**), 40% (**19**, **20**, **21**), and 50% (**16**, **18**, **28**, **35**) thermal ellipsoid probability.

dx.doi.org/10.1021/jo5004482 | J. Org. Chem. 2014, 79, 3973–3981

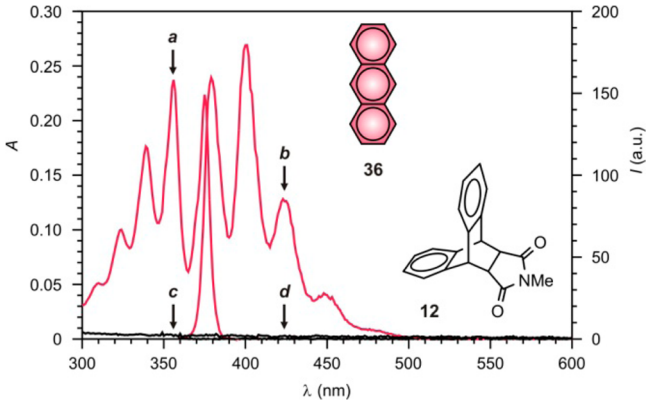

Figure 5. Absorption and emission spectra (MeCN, 25 °C, λ_{Ex} = 350 nm) of **36** (30 μM, a and b) and **12** (0.1 mM, c and d).

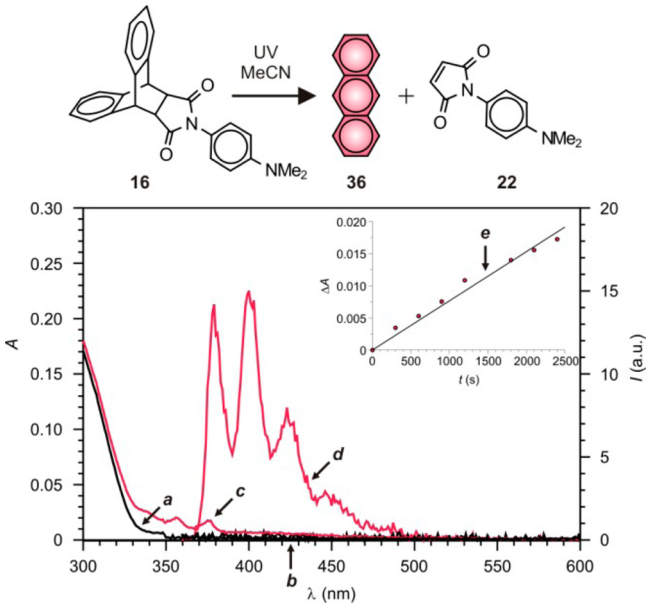

Figure 6. Absorption and emission spectra of **16** (20 μM, MeCN, 25 °C, λ_{Ex} = 350 nm) before (a and b) and after (c and d) ultraviolet (UV) irradiation (254 nm, 0.4 mW cm^{-2}, 40 min) and the corresponding absorbance evolution at 355 nm during photolysis.

evolution at 355 nm during photolysis indicates the quantum yield (ϕ_P in Table 1) for this photochemical transformation to be 0.001.[32] In contrast to the behavior of **16**, illumination of **17** does not result in the formation of **36**. Instead of the anthracene bands, an absorption centered at 359 nm together with a weak and broad emission appear in the spectra recorded after relatively short irradiation times (a–d in Figure S13, Supporting Information).

The absorption spectrum (Figure 7, a) of **12** indicates the molar extinction coefficient (ε) to be less than 1 mM^{-1} cm^{-1} between 240 and 300 nm. The introduction of a 4-(dimethylamino)phenyl chromophore on the maleimide bridge, in the shape of **16**, translates into the appearance of an intense band within this range of wavelengths with a ε of 21 mM^{-1} cm^{-1} at 264 nm (Figure 7, b). These observations indicate that this particular chromophoric fragment is mainly responsible for absorbing the exciting photons and initiating the photochemical transformation of **16** into **22** and **36**.

Density functional theory (DFT) calculations assign the main band of **16** to a $S_0 \rightarrow S_6$ transition (Figure 7) with

Table 1. Quantum Yield (ϕ_P) for the Photochemical Retro-cycloadditions and Fluorescence Quantum Yield (ϕ_F) of the Resulting Anthracenes[a]

	ϕ_P	ϕ_F
16 → **36**	0.001	0.27
28 → **25**	0.01	0.07
34 → **30**	0.001	0.43
35 → **31**	0.002	0.85

[a]All measurements were performed in aerated MeCN at 25 °C. Samples were illuminated at 254 nm. The irradiation power per unit area (0.4 mW cm^{-2}) was measured with a potassium ferrioxalate actinometer, and this value was used to determine ϕ_P from the corresponding absorbance evolution during photolysis, according to an established procedure (ref 33). The values of ϕ_F listed for **25**, **30**, and **36** are literature data (ref 35), and that of **31** was determined against an EtOH solution of 9,10-diphenylanthracene. The value of ϕ_F for this standard is 0.95 (ref 34).

estimated wavelength (λ_{Cal}) and oscillator strength (f_{Cal}) of 259 nm and 0.179 respectively (Table S3, Supporting Information). Instead, λ_{Cal} for the $S_0 \rightarrow S_1$ transition is 321 nm with a f_{Cal} of only 0.004, in agreement with the presence of a relatively weak band in the experimental spectrum (Figure 7, b) at this wavelength. Visualization of the main orbital pair responsible for this electronic transition reveals that the highest-occupied molecular orbital (HOMO in Figure 7) is mostly localized on the 4-(dimethylamino)phenyl ring, while the lowest unoccupied molecular orbital (LUMO in Figure 7) is predominantly on the imide group. In fact, the orthogonal arrangement of one relative to the other, evident also in the crystal structure (Figure 4), isolates electronically the two groups in the ground state. Thus, the population of S_1 results essentially in the formal transfer of one electron from the 4-(dimethylamino)phenyl ring to the imide group.

The dissociation of adduct **16** into diene **36** and dienophile **22** can be simulated by elongating stepwise one of the two [C–C] bonds joining the anthracene and maleimide fragments. The energies for S_0, S_1, and T_1 of the optimized geometries at each step can then be plotted against the bond length to build the reaction profiles illustrated in Figure 8. In S_0, the energy increases monotonically and dramatically with bond length in full agreement with experiments, which did not reveal any thermal dissociation of the cycloadduct into its constituent components even after heating for prolonged time.[32] In fact, frequency calculations indicate the free energy of the transition state, found along this reaction path, to be 33.94 kcal mol^{-1} greater than that of **16** (Figure 9). Instead, the free energy of the two separate products is only 3.67 kcal mol^{-1} higher than that of the cycloadduct.

In contrast to the reaction profile in S_0 (Figure 8), the energy remains almost constant in S_1 (ΔE < 0.2 eV) and, after a modest initial increase (ΔE = 0.6 eV), decreases significantly in T_1. Thus, the retro-cycloaddition of **16** into **22** and **36** can, indeed, proceed photochemically, and it can evolve along the potential energy surface of either one of these two excited states. Presumably, ultraviolet illumination of **16** results predominantly in the population of S_6 (Figure 7). Then, **16** can decay to S_1, after internal conversion, and either dissociate along the relatively flat potential energy surface of this state or undergo intersystem crossing and dissociate in T_1.

Adducts **12**–**21** differ exclusively in the nature of their maleimide bridge. Their spectroscopic analysis, together with the DFT calculations on **16**, indicate that a 4-(dimethylamino)-

dx.doi.org/10.1021/jo5004482 | J. Org. Chem. 2014, 79, 3973–3981

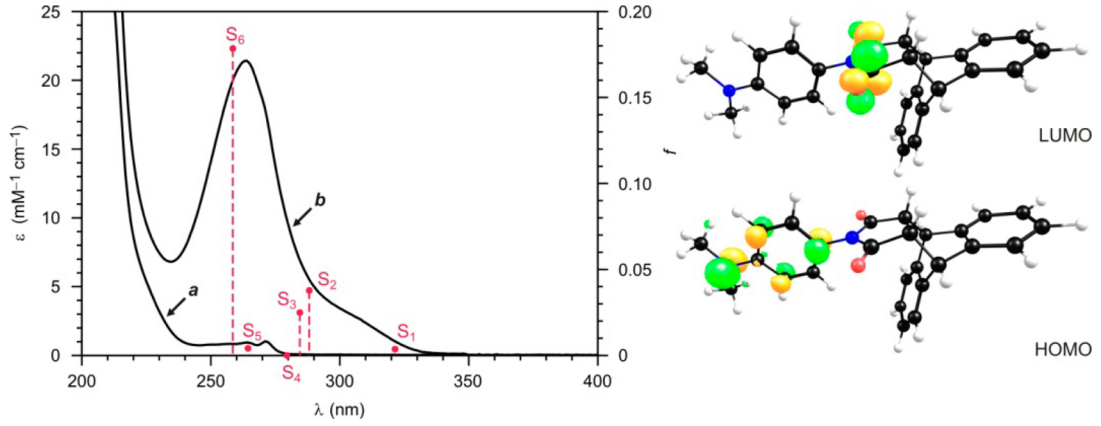

Figure 7. Experimental absorption spectra (MeCN, 25 °C) of **12** (a) and **16** (b) together with calculated [B3LYP/6-311+G(d,p), IEFPCM for MeCN] singlet excited states of **16** and isosurfaces for the main orbital pair associated with the $S_0 \rightarrow S_1$ transition.

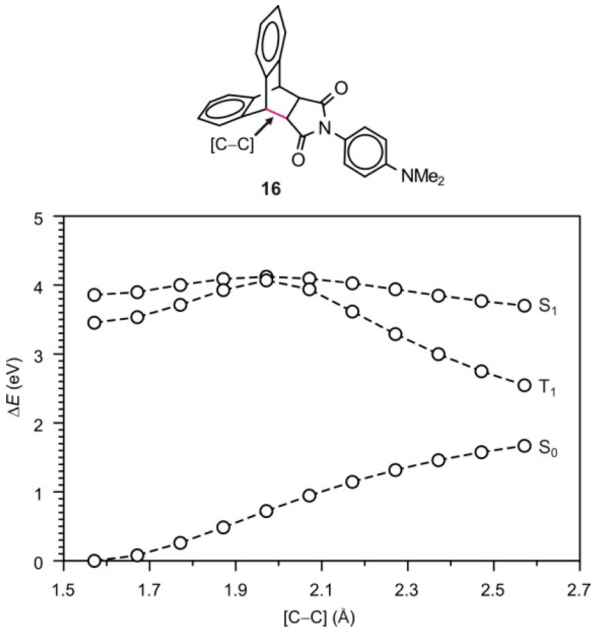

Figure 8. Relative energies [B3LYP/6-311+G(d,p), IEFPCM for MeCN] of **16** in S_0, S_1, and T_1 against the length of one of the two [C–C] bonds joining the anthracene and maleimide fragments.

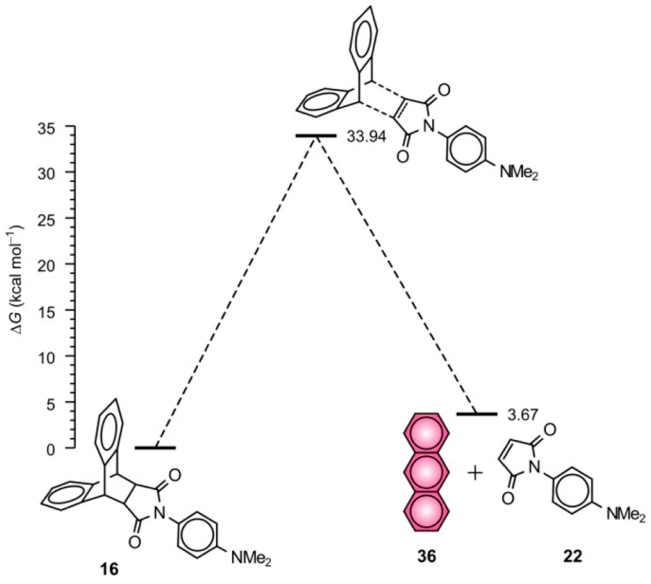

Figure 9. Relative free energies [B3LYP/6-311+G(d,p), IEFPCM for MeCN] of adduct **16**, products **22** and **36**, and the corresponding transition state.

phenyl group is essential on the bridging unit for the photochemical dissociation of these adducts to occur. Adducts **26**–**28**, **34**, and **35** all have this particular group on their maleimide bridge and differ instead in the substituents on the anthracene fragment. In all instances, ultraviolet illumination results in significant changes in absorption and emission. The spectra (Figures S14 and S15, Supporting Information) of **26** and **27**, however, do not reveal the characteristic band of the corresponding anthracene drivatives after irradiation. Instead, an absorption at ca. 355 nm together with a broad and weak emission appear for both compounds. These bands resemble the ones detected for **17** (Figure S13, Supporting Information). All three cycloadducts have iodide substituents and such heavy atoms are known to encourage intersystem crossing.[35] Presumably, a photochemical pathway in competition with the expected retro-cycloaddition is promoted for all three compounds via the efficient population on the corresponding triplet states.

In contrast to the behavior of **26** and **27**, cycloadducts **28**, **34**, and **35** undergo photoinduced retro-cycloaddition. In all instances, the characteristic absorption and emission bands (Figures S16–S18, Supporting Information) of the corresponding anthracene derivatives develop under illumination. Plots of the absorbance evolution during photolysis indicates ϕ_P to range from 0.001 up to 0.01 (Table 1). Interestingly, ϕ_P of **28** is 1 order of magnitude greater than those of **16**, **34**, and **35**. Presumably, the steric hindrance associated with the two bromine substituents on the bridgehead carbon atoms of **28** facilitates the dissociation of this particular adduct into the corresponding diene and dienophile. By contrast, the introduction of a pair of methoxy or phenylethynyl substituents on the two *o*-phenylene rings, in the shape of **34** or **35**, respectively, has negligible influence on ϕ_P, which remains almost identical to that of **16**. Nonetheless, the two phenylethynyl groups have a pronounced influence on the fluorescence quantum yield (ϕ_F in Table 1) of the photochemical product. Indeed, **31** has the greatest ϕ_F out of the four photoactivatable anthracenes investigated and, therefore, is the

dx.doi.org/10.1021/jo5004482 | J. Org. Chem. 2014, 79, 3973–3981

best candidate for possible imaging applications based on this family of photoactivatable fluorophores.[36]

CONCLUSIONS

The reaction of the maleic anhydride cycloadduct of anthracene with substituted anilines offers convenient synthetic access to the corresponding maleimide cycloadducts in good yields. In the resulting compounds, the maleimide bridge, across positions 9 and 10 of the oligoacene platform, isolates the peripheral *o*-phenylene rings and suppresses the characteristic absorption and emission bands of the anthracene chromophore. When a 4-dimethylamino group is attached to the nitrogen atom of the maleimide bridge, ultraviolet illumination results in retro-cycloaddition with a quantum yield of 0.001 to regenerate anthracene and its spectroscopic signature. The 4-dimethylamino appendage collects the exciting photons effectively and encourages the population of the excited state responsible for the photochemical regeneration of anthracene. The introduction of substituents, in the form of a pair of bromine atoms, on the bridgehead carbon atoms of the *N*-4-(dimethylamino)-maleimide cycloadduct facilitates the photochemical transformation and brings the corresponding quantum yield up to 0.01. Instead, the presence of substituents on the peripheral *o*-phenylene rings of the cycloadduct has negligible influence on the quantum efficiency of the photochemical process. These groups, however, can be exploited to regulate the photophysical properties of the photochemical product. When a pair of phenylethynyl groups are attached to positions 2 and 8 of the anthracene chromophore the fluorescence quantum yields raises up to 0.85. Thus, these particular operating principles provide the possibility to convert photochemically a non-fluorescent reactant into a fluorescent product and, hence to activate fluorescence efficiently under the influence of optical stimulations. As a result, this structural design can evolve into the realization of valuable molecular probes for imaging applications based on fluorescence photoactivation.

EXPERIMENTAL SECTION

Materials and Methods. Chemicals were purchased from commercial sources and used as received with the exception of MeCN, which was distilled over CaH_2. Compounds **1**, **12**−**15**, **22**, and **30**−**32** were prepared according to literature procedures.[30−39] Electrospray ionization mass spectra (ESIMS) were recorded with a TOF-Q spectrometer. NMR spectra were recorded with 300 and 400 MHz spectrometers. Absorption spectra were recorded in quartz cells with a path length of 1.0 cm. Emission spectra were recorded in aerated solutions. The value of ϕ_F for **31** was determined with a 9,10-diphenylanthracene standard, following a literature protocol.[40] Solutions were irradiated either at 254 nm (0.4 mW cm^{-2}) or at 350 nm (2.5 mW cm^{-2}). The values of ϕ_P were determined with a potassium ferrioxalate actinometer, according to an established procedure.[33]

General Procedure for the Synthesis of 16−21. An equimolar solution of **1** (138 mg, 0.5 mmol) and the corresponding amine (**2**−**11**) in MeCN (5 mL) was heated under reflux for 16 h over K_2CO_3 (112 mg, 0.8 mmol). After being cooled to ambient temperature, the mixture was diluted with CH_2Cl_2 (30 mL) and washed with H_2O (20 mL). The combined organic layers were dried over Na_2SO_4, the solvent was distilled off under reduced pressure, and the residue was purified by column chromatography (SiO_2).

16: AcOEt/hexanes (1.5:3.5, v/v); white solid (120 mg, 60%); ESIMS m/z = 395.1758 $[M + H]^+$ (m/z calcd for $C_{26}H_{23}N_2O_2$ = 395.1761); ^1H NMR (CD_3CN) δ = 2.88 (6H, s), 3.23 (2H, s), 4.82 (2H, s), 6.23 (2H, d, 9 Hz), 6.59 (2H, d, 9 Hz), 7.18−7.26 (4H, m), 7.28−7.33 (2H, m), 7.44−7.51 (2H, m); ^{13}C NMR ($CDCl_3$) δ = 40.8, 46.3, 47.3, 112.8, 120.1, 124.7, 125.6, 127.2, 127.4, 127.5, 139.2, 141.8, 150.9, 177.2.

17: AcOEt/hexanes (1:4, v/v); yellow solid (80 mg, 32%); ESIMS m/z = 478.0296 $[M + H]^+$ (m/z calcd for $C_{24}H_{17}INO_2$ = 478.0305); ^1H NMR ($CDCl_3$) δ = 3.38 (2H, s), 4.89 (2H, s), 6.29 (2H, d, 8 Hz), 7.19−7.24 (4H, m), 7.32−7.36 (2H, m), 7.41−7.45 (2H, m), 7.64 (2H, d, 8 Hz); ^{13}C NMR ($CDCl_3$) δ = 46.3, 47.5, 80.0, 94.8, 117.7, 124.8, 125.5, 127.3, 127.6, 128.5, 131.4, 138.3, 138.7, 139.1, 141.5, 146.5, 176.2.

18: AcOEt/hexanes (3:2, v/v); white solid (130 mg, 63%); ESIMS m/z = 434.1375 $[M + Na]^+$ (m/z calcd for $C_{26}H_{21}NO_4Na$ = 434.1368); ^1H NMR ($CDCl_3$) δ = 3.38 (2H, s), 3.72 (3H, s), 3.82 (3H, s), 4.90 (2H, s), 5.73 (1H, s), 6.14 (1H, d, 9 Hz), 6.76 (1H, d, 9 Hz), 7.19−7.24 (4H, m), 7.33−7.39 (2H, m), 7.40−7.46 (2H, m); ^{13}C NMR ($CDCl_3$) δ = 46.3, 47.4, 56.4, 110.1, 111.4, 119.5, 124.4, 124.8, 125.6, 127.3, 127.4, 139.4, 141.6, 149.6, 149.7, 176.9.

19: AcOEt/hexanes (1:4, v/v); white solid (92 mg, 46%); ESIMS m/z = 424.1302 $[M + Na]^+$ (m/z calcd for $C_{28}H_{19}NO_2Na$ = 424.1313); ^1H NMR (CD_3CN) δ = 3.56 (2H, s), 4.95 (2H, s), 5.32 (1H, d, 8 Hz), 7.16−7.31 (4H, m), 7.40−7.56 (8H, m), 7.88−7.90 (1H, m), 7.94 (1H, d, 8 Hz); ^{13}C NMR ($CDCl_3$) δ = 45.9, 46.4, 47.8, 47.9, 122.3, 124.7, 124.8, 125.6, 125.7, 126.2, 126.3, 126.8, 127.3, 127.4, 127.7, 127.9, 128.5, 128.9, 129.5, 130.2, 130.4, 134.5, 139.4, 139.9, 141.7, 142.2, 176.7, 176.8.

20: AcOEt/CH_2Cl_2 (1:4, v/v); white solid (82 mg, 38%); ESIMS m/z = 434.1376 $[M + H]^+$ (m/z calcd for $C_{28}H_{20}NO_4$ = 434.1394); ^1H NMR ($CDCl_3$) δ = 2.40 (3H, s), 3.43 (2H, s), 4.91 (2H, s), 6.29 (1H, s), 6.58 (1H, s), 7.21−7.26 (4H, m), 7.33−7.39 (2H, m), 7.42−7.47 (2H, m), 7.54 (2H, d, 8 Hz); ^{13}C NMR ($CDCl_3$) δ = 19.0, 30.1, 46.3, 47.5, 115.6, 116.1, 120.4, 122.5, 124.8, 125.5, 127.4, 127.8, 134.5, 139.0, 141.4, 151.9, 153.8, 160.5, 175.9.

21: AcOEt/hexanes (2:3, v/v); white solid (85 mg, 36%); ESIMS m/z = 491.1724 $[M + Na]^+$ (m/z calcd for $C_{32}H_{24}N_2O_2Na$ = 491.1735); ^1H NMR (CD_3CN) δ = 1.34 (3H, t, 6 Hz), 3.43 (2H, s), 4.38 (2H, q, 6 Hz), 4.89 (2H, s), 6.48 (1H, d, 9 Hz), 7.03 (1H, s), 7.20−7.27 (3H, m), 7.31−7.45 (5H, m), 7.47−7.56 (4H, m), 8.00 (1H, d, 9 Hz); ^{13}C NMR ($CDCl_3$) δ = 13.8, 37.6, 46.0, 47.1, 50.9, 108.7, 108.9, 119.0, 119.2, 120.6, 122.4, 123.3, 123.7, 124.4, 125.3,126.2, 126.9, 127.2, 139.0, 139.6, 140.3, 141.4, 177.1.

General Procedure for Synthesis of 26−28. An equimolar solution of **22** (108 mg, 0.5 mmol) and the corresponding anthracene derivative (**23**−**25**) in *m*-xylene (5 mL) was heated under reflux for 16 h. After the solution was cooled to ambient temperature, the solvent was distilled off under reduced pressure and the residue was purified by column chromatography (SiO_2).

26: AcOEt/hexanes (1:4 v/v); yellow solid (116 mg, 36%); ESIMS m/z = 646.9717 $[M + H]^+$ (m/z calcd for $C_{26}H_{21}I_2N_2O_2$ = 646.9694); ^1H NMR (CD_3CN) δ = 2.92 (6H, s), 3.35 (2H, s), 4.79 (2H, s), 6.29 (2H, d, 8 Hz), 6.65 (2H, d, 8 Hz), 7.11 (1H, d, 8 Hz), 7.27 (1H, d, 8 Hz), 7.61 (2H, t, 8 Hz), 7.70 (1H, s), 7.86 (1H, s); ^{13}C NMR ($CDCl_3$) δ = 40.9, 45.3, 45.4, 46.6, 46.9, 92.4, 92.7, 112.9, 126.6, 127.3, 127.4, 133.8, 134.3, 136.4, 136.7, 138.3, 140.8, 141.1, 143.6, 151.0, 151.2, 176.4.

27: AcOEt/hexanes (2:3 v/v); yellow solid (178 mg, 55%); ESIMS m/z = 646.9692 $[M + H]^+$ (m/z calcd for $C_{26}H_{21}I_2N_2O_2$ = 646.9694); ^1H NMR (CD_3CN) δ = 2.90 (6H, s), 3.36 (2H, s), 4.86 (1H, s), 5.48 (1H, s), 6.30 (2H, d, 6 Hz), 6.63 (2H, d, 6 Hz), 6.99 (2H, t, 6 Hz), 7.33 (1H, d, 6 Hz), 7.48 (1H, d, 9 Hz), 7.68−7.77 (2H, m); ^{13}C NMR ($CDCl_3$) δ = 40.8, 46.1, 46.6, 47.9, 53.6, 95.3, 96.3, 112.8, 120.0, 124.6, 125.6, 127.3, 129.2, 129.3, 137.5, 137.8, 143.0, 143.5, 144.9, 150.9, 175.4, 176.6.

28: AcOEt/hexanes (2:3 v/v); yellow solid (105 mg, 38%); ESIMS m/z = 552.9945 $[M + H]^+$ (m/z calcd for $C_{26}H_{21}Br_2N_2O_2$ = 552.9949); ^1H NMR (CD_3CN) δ = 2.91 (6H, s), 3.64 (2H, s), 6.40 (2H, d, 8 Hz), 6.57 (2H, d, 8 Hz), 7.35−7.43 (4H, m), 7.79−7.83 (2H, m), 7.98−8.03 (2H, m); ^{13}C NMR ($CDCl_3$) δ = 40.8, 55.4, 64.3, 112.5, 119.9, 125.9, 125.9, 127.2, 128.7, 129.0, 137.2, 140.1, 150.9, 171.8.

dx.doi.org/10.1021/jo5004482 | J. Org. Chem. 2014, 79, 3973−3981

Synthesis of 33. A solution of **29** (40 mg, 0.4 mmol) and **31** (150 mg, 0.4 mmol) in *m*-xylene (5 mL) was heated under reflux for 16 h. After being cooled to ambient temperature, the mixture was cooled further with an ice bath and the resulting precipitate was filtered off. The solid residue was washed with hexane and then crystallized with *m*-xylene to give **33** (80 mg, 42%) as a white solid: ESIMS m/z = 499.1293 $[M + Na]^+$ (m/z calcd for $C_{34}H_{20}O_3Na$ = 499.1310); ^1H NMR (CD_3CN) δ = 3.68−3.74 (1H, m), 3.77−3.83 (1H, m), 5.00 (1H, s), 5.96 (1H, s), 7.19−7.32 (6H, m), 7.34−7.54 (10H, m); ^{13}C NMR ($CDCl_3$) δ = 41.5, 46.1, 47.5, 48.1, 86.0, 86.1, 94.2, 94.3, 120.4, 121.3, 122.9, 123.3, 124.6, 125.5, 127.4, 127.9, 128.7, 128.8, 128.9, 131.0, 131.5, 132.2, 132.3, 138.9, 139.5, 141.4, 141.9, 144.7, 169.8, 170.8.

General Procedure for the Synthesis of 34 and 35. An equimolar solution of **6** (0.2 mmol) and the corresponding anthracene derivative (**32** or **33**) in MeCN (5 mL) was heated under reflux for 16 h over K_2CO_3 (42 mg, 0.3 mmol). After being cooled to ambient temperature, the mixture was diluted with CH_2Cl_2 (30 mL) and washed with H_2O (20 mL). The combined organic layers were dried over Na_2SO_4, the solvent as distilled off under reduced pressure, and the residue was purified by column chromatography [SiO_2, AcOEt/hexanes (2:3, v/v)] to give the product.

34: white solid (50 mg, 55%); ESIMS m/z = 455.1975 $[M + H]^+$ (m/z calcd for $C_{28}H_{27}N_2O_4$ = 455.1973); ^1H NMR (CD_3CN) δ = 2.90 (6H, s), 3.29 (2H, s), 3.76 (3H, s), 3.78 (3H, s), 4.71 (2H, s), 6.30 (2H, d, 8 Hz), 6.63 (2H, d, 8 Hz), 6.74 (2H, t, 8 Hz), 6.89 (1H, s), 7.07 (1H, s), 7.19 (1H, d, 8 Hz), 7.35 (1H, d, 8 Hz); ^{13}C NMR ($CDCl_3$) δ = 40.8, 45.8, 47.4, 47.6, 55.9, 56.0, 111.2, 111.4, 112.6, 112.8, 120.2, 120.3, 125.4, 126.3, 127.4, 131.1, 133.8, 141.1, 143.8, 150.9, 158.9, 159.3, 177.1, 177.3.

35: white solid (40 mg, 45%); ESIMS m/z = 595.2409 $[M + H]^+$ (m/z calcd for $C_{42}H_{31}N_2O_2$ = 595.2387); ^1H NMR [$(CD_3)_2CO$] δ = 2.90 (6H, s), 3.47−3.51 (1H, m), 3.53−3.57 (1H, m), 5.01 (1H, s), 6.03 (1H, s), 6.42 (2H, d, 8 Hz), 6.60 (2H, d, 8 Hz), 7.16−7.20 (2H, m), 7.26−7.35 (5H, m), 7.37−7.48 (6H, m), 7.55−7.63 (3H, m); ^{13}C NMR ($CDCl_3$) δ = 29.7, 40.4, 41.6, 46.0, 46.2, 46.6, 86.1, 86.3, 112.5, 119.9, 120.7, 122.7, 123.2, 124.2, 125.1, 126.6, 126.8, 127.0, 128.2, 128.3, 130.3, 130.4, 131.8, 132.0, 139.2, 140.0, 141.8, 142.3, 150.5, 175.5, 176.5.

Crystallographic Analysis. Single crystals of **15**, **18**, and **21** were obtained after diffusion of Et_2O vapors into a CH_2Cl_2 solution of the corresponding compound. Single crystals of **16** were obtained after diffusion of hexane vapors into a $CHCl_3$ solution of the compound. Single crystals of **19** and **28** were obtained after diffusion of Et_2O vapors into a $CHCl_3$ solution of the corresponding compound. Single crystals of **20** were obtained after diffusion of hexane/Et_2O (2:1, v/v) vapors into a $CHCl_3$ solution of the compound. Single crystals of **34** were obtained after diffusion of Et_2O vapors into an EtOAc solution of the compound. Single crystals of **35** were obtained after diffusion of hexane vapors into a MeCN solution of the compound. The data crystal of **15**, **16**, **18**−**21**, and **34** was glued onto the end of a thin glass fiber. The data crystals of **28** and **35** were mounted onto the end of a thin glass fiber using Paratone-N for data collection at 100 K under flow of N_2. X-ray intensity data were measured with a CCD-based diffractometer, using Mo Kα radiation (λ = 0.71073 Å).[41] The raw data frames were integrated with a narrow-frame integration algorithm. Corrections for Lorentz and polarization effects were applied. An empirical absorption correction based on the multiple measurement of equivalent reflections was applied. The structures were solved by a combination of direct methods and difference Fourier syntheses and refined by full-matrix least-squares on F^2.[42] All non-hydrogen atoms were refined with anisotropic displacement parameters. Hydrogen atoms were placed in geometrically idealized positions and included as standard riding atoms during the least-squares refinements. Crystal data, data collection parameters, and results of the analyses are listed in Tables S1−S3 (Supporting Information).

Compounds **15**, **16**, **20**, **21**, **34**, and **35** crystallized in the triclinic crystal system. The space group $P\bar{1}$ was assumed and confirmed by the successful refinement and solution of the structures. For compound **15**, two molecules are present in the asymmetric crystal unit. One molecule of MeCN cocrystallized with **35**. The solvent molecule was included in the analysis and refined with anisotropic thermal parameters. Compound **18** crystallized in the orthorhombic crystal system. The systematic absences in the intensity data identified the unique space group $P2_12_12_1$. Compounds **19** and **28** crystallized in the monoclinic crystal system. The systematic absences in the intensity data identified the unique space group $P2_1/n$.

Computational Methods. Density-functional theory[43] (DFT) calculations were performed with the 6-311+G(d,p) basis set and the restricted B3LYP[44,45] functional implemented in Gaussian 09.[46] Geometry optimizations, frequencies, molecular orbitals, and excited states were computed with the polarizable continuum model (PCM) for acetonitrile using the integral equation formalism (IEF) variant.[47]

The geometry adopted by **16** in single crystals (Figure 4) was optimized. No imaginary frequencies were found for the optimized structure. Molecular orbitals and the first 10 singlet excited states were computed for this geometry (HOMO, LUMO and S_1−S_6 in Figure 7). The [C−C] bond between one of the two bridgehead carbon atoms and the corresponding maleimide carbon atom was elongated in 20 consecutive steps of 0.1 Å each. The remaining coordinates were optimized at each step and the first 5 singlet and 5 triplet excited states of each optimized geometry were computed.[48,49] The energies of S_0, S_1, and T_1 of each optimized geometry were plotted against the corresponding [C−C] distances (Figure 8). The geometry with highest S_0 energy (step 12) was optimized to a transition state with no distance constraint. One imaginary frequency (video S1, Supporting Information) was found. The last geometry of the distance scan (step 20) shows the two separate products (**22** and **36**) was optimized further with no distance constraint. No imaginary frequencies were found. The free energies of transition state and products were computed relative to that of the very first geometry of the distance scan (Figure 8).

■ ASSOCIATED CONTENT

Supporting Information

^1H and ^{13}C NMR spectra of **16**−**21**, **26**−**28**, and **33**−**35**; crystallographic data for **15**, **16**, **18**−**21**, **28**, **34**, and **35**; absorption and emission spectra of **17**, **26**−**28**, **34**, and **35**; computed coordinates of **16**, **22**, **36**, and the corresponding transition state; animation of the vibration associated with the imaginary frequency of the transition state. This material is available free of charge via the Internet at http://pubs.acs.org.

■ AUTHOR INFORMATION

Corresponding Author

*E-mail: fraymo@miami.edu.

Notes

The authors declare no competing financial interest.

■ ACKNOWLEDGMENTS

The National Science Foundation (CAREER Award CHE-0237578, CHE-0749840, and CHE-1049860) is acknowledged for financial support.

■ REFERENCES

(1) Mitchison, T. J.; Sawin, K. E.; Theriot, J. A.; Gee, K.; Mallavarapu, A. *Methods Enzymol.* **1998**, *291*, 63−78.

(2) Wysocki, L. M.; Davis, L. D. *Curr. Opin. Chem. Biol.* **2011**, *15*, 752−759.

(3) Puliti, D.; Warther, D.; Orange, C.; Specht, A.; Goeldner, M. *Bioorg. Med. Chem.* **2011**, *19*, 1023−1029.

(4) Li, W.-H.; Zheng, G. *Photochem. Photobiol. Sci.* **2012**, *11*, 460−471.

(5) Klán, P.; Šolomek, T.; Bochet, C. G.; Blanc, A.; Givens, R.; Rubina, M.; Popik, V.; Kostikov, A.; Wirz, J. *Chem. Rev.* **2013**, *113*, 119−191.

(6) Raymo, F. M. *Phys. Chem. Chem. Phys.* **2013**, *15*, 14840−14850.
(7) Adams, S. R.; Tsien, R. Y. *Annu. Rev. Physiol.* **1993**, *55*, 755−784.
(8) Politz, J. C. *Trends Cell Biol.* **1999**, *9*, 284−287.
(9) Dirks, R. W.; Molenaar, C.; Tanke, H. J. *Histochem. Cell Biol.* **2001**, *115*, 3−11.
(10) Ellis-Davies, G. C. *Nat. Methods* **2007**, *4*, 619−628.
(11) Xu, Y.; Melia, T. J.; Toomre, D. T. *Curr. Opin. Chem. Biol.* **2011**, *15*, 822−830.
(12) Raymo, F. M. *ISRN Phys. Chem.* **2012**, 619251−1−15.
(13) Huang, B.; Bates, M.; Zhuang, X. *Annu. Rev. Biochem.* **2009**, *78*, 993−1016.
(14) Hell, S. W. *Nat. Methods* **2009**, *6*, 24−32.
(15) van de Linde, S.; Heilemann, M.; Sauer, M. *Annu. Rev. Phys. Chem.* **2012**, *63*, 519−540.
(16) Ha, T.; Tinnefeld, P. *Annu. Rev. Phys. Chem.* **2012**, *63*, 595−617.
(17) Moerner, W. E. *J. Microsc.* **2012**, *246*, 213−220.
(18) Raymo, F. M. *J. Phys. Chem. Lett.* **2012**, *3*, 2379−2385.
(19) (a) Zweig, A. *Pure Appl. Chem.* **1973**, *33*, 389−410. (b) Zweig, A.; Huffman, K. R.; Gallivan, J. B.; Orloff, M. K.; Halverson, F. *J. Am. Chem. Soc.* **1974**, *96*, 1449−1458.
(20) Baro, J.; Dudek, D.; Luther, K.; Troe, J. *Zeit. Phys. Chem.* **1984**, *140*, 167−179.
(21) Strating, J.; Zwanenburg, B.; Wagenaar, A.; Udding, A. C. *Tetrahedron Lett.* **1969**, *10*, 125−128.
(22) Ihlemann, J.; Bolle, M.; Luther, K.; Troe, J. *Proc. SPIE* **1991**, *1361*, 1011−1019.
(23) (a) Mondal, R.; Shah, B. K.; Neckers, D. C. *J. Am. Chem. Soc.* **2006**, *128*, 9612−9613. (b) Mondal, R.; Adhikari, R. M.; Shah, B. K.; Neckers, D. C. *Org. Lett.* **2007**, *9*, 2505−2508. (c) Zhao, Y.; Mondal, R.; Neckers, D. C. *J. Org. Chem.* **2008**, *73*, 5506−5513. (d) Mondal, R.; Okhrimenko, A. N.; Shah, B. K.; Neckers, D. C. *J. Phys. Chem. B* **2008**, *112*, 11−15. (e) Mondal, R.; Tönshoff, C.; Khon, D.; Neckers, D. C.; Bettinger, H. F. *J. Am. Chem. Soc.* **2009**, *131*, 14281−14289. (f) Zhao, Y.; Cai, X.; Danilov, E.; Li, G.; Neckers, D. C. *Photochem. Photobiol. Sci.* **2009**, *8*, 34−36. (g) Tönshoff, C.; Bettinger, H. F. *Angew. Chem., Int. Ed.* **2010**, *48*, 4125−4128. (h) Bettinger, H. F.; Mondal, R.; Krasowska, M.; Neckers, D. C. *J. Org. Chem.* **2013**, *78*, 1851−1857.
(24) (a) Uno, H.; Yamashita, Y.; Kikuchi, M.; Watanabe, H.; Yamada, H.; Okujima, T.; Ogawa, T.; Ono, N. *Tetrahedron Lett.* **2005**, *46*, 1981−1983. (b) Yamada, H.; Yamashita, Y.; Kikuchi, M.; Watanabe, H.; Okujima, T.; Uno, H.; Ogawa, T.; Ohara, K.; Ono, N. *Chem.—Eur. J.* **2005**, *11*, 6212−6220. (c) Yamada, H.; Kawamura, E.; Sakamoto, S.; Yamashita, Y.; Okujima, T.; Uno, H.; Ono, N. *Tetrahedron Lett.* **2006**, *47*, 7501−7504. (d) Masumoto, A.; Yamashita, Y.; Go, S.; Kikuchi, T.; Yamada, H.; Okujima, T.; Ono, N.; Uno, H. *Jpn. J. Appl. Phys.* **2009**, *48*, 051505−1−5. (e) Yamada, H.; Kuzuhara, D.; Ohkubo, K.; Takahashi, T.; Okujima, T.; Uno, H.; Ono, N.; Fukuzumi, S. *J. Mater. Chem.* **2010**, *20*, 3011−3024. (f) Katsuta, S.; Yamada, H.; Okujima, T.; Uno, H. *Tetrahedron Lett.* **2010**, *51*, 1397−1400. (g) Aotake, T.; Ikeda, S.; Kuzuhara, D.; Mori, S.; Okujima, T.; Uno, H.; Yamada, H. *Eur. J. Org. Chem.* **2012**, 1723−1729. (h) Aotake, T.; Tanimoto, H.; Hotta, H.; Kuzuhara, D.; Okujima, T.; Uno, H.; Yamada, H. *Chem. Commun.* **2013**, *49*, 3661−3663. (i) Aotake, T.; Yamashita, Y.; Okujima, T.; Shirasawa, N.; Jo, Y.; Fujimori, S.; Uno, H.; Ono, N.; Yamada, H. *Tetrahedron Lett.* **2013**, *54*, 1790−1793. (j) Suzuki, M.; Aotake, T.; Yamaguchi, Y.; Noguchi, N.; Nakano, H.; Nakayama, K.; Yamada, H. *J. Photochem. Photobiol. C* **2014**, *18*, 50−70.
(25) Peng, P.; Wang, C. M.; Shi, Z.; Johns, V. K.; Ma, L. Y.; Oyer, J.; Copik, A.; Igarashi, R.; Liao, Y. *Org. Biomol. Chem.* **2013**, *11*, 6671−6674.
(26) Nozaki, H.; Kato, H.; Noyori, R. *Tetrahedron* **1969**, *25*, 1661−1665.
(27) Atherton, J. C. C.; Jones, S. *Tetrahedron Lett.* **2002**, *43*, 9097−9100.
(28) (a) Adachi, Y.; Nakagawa, H.; Matsuo, K.; Suzuki, T.; Miyata, N. *Chem. Commun.* **2008**, 5149−5151. (b) Matsuo, K.; Nakagawa, H.; Adachi, Y.; Kameda, E.; Tsumoto, H.; Suzuki, T.; Miyata, N. *Chem. Commun.* **2010**, 3788−3790.
(29) Johns, V. K.; Shi, Z.; Dang, W.; McInnis, M. D.; Weng, Y.; Liao, Y. *J. Phys. Chem. A* **2011**, *115*, 8093−8099.
(30) Rani, R.; Arya, S.; Kilaru, P.; Sondhi, S. M. *Green Chem. Lett. Rev.* **2012**, *5*, 545−575.
(31) Synthetic procedures for the preparation of **12**−**15** and **32** are reported in ref 29 and in: Weber, E.; Finge, S.; Csoeregh, I. *J. Org. Chem.* **1991**, *56*, 7281−7288.
(32) The absorption and emission spectra of an acetonitrile solution of **16** do not reveal any change even after heating under reflux for 6 h in the dark. Thus, this particular cycloadduct is thermally stable and dissociates into its constituent components only under ultraviolet illumination.
(33) Scaiano, J. C. *Handbook of Organic Photochemistry*; CRC Press: FL, 1989.
(34) Morris, J. V.; Mahaney, M. A.; Hube, J. R. *J. Phys. Chem.* **1976**, *80*, 969−974.
(35) Turro, N. J.; Ramamurthy, V.; Scaiano, J. C. *Principles of Molecular Photochemistry: An Introduction*; University Science Books: Sausalito, 2009.
(36) The values of ϕ_F for **25**, **30**, and **36** are reported in: (a) Dawson, W. R.; Windsor, M. W. *J. Phys. Chem.* **1968**, *72*, 3251−3260. (b) Favaro, G.; di Nunzio, M. R.; Gentili, P. L.; Romani, A.; Becker, R. S. *J. Phys. Chem. A* **2007**, *111*, 5948−5953. (c) Zhou, X.; Piland, G. B.; Kurunthu, D.; Dillon, R. J.; Burdett, J. J.; Bardeen, C. J. *J. Lumin.* **2012**, *132*, 2997−3003.
(37) Cai, H.; He, X.-H.; Zheng, D.-Y.; Qiu, J.; Li, Z.-C.; Li, F.-M. *J. Polym. Sci., Part A* **1996**, *34*, 1245−1250.
(38) Goichi, M.; Segawa, K.; Suzuki, S.; Toyota, S. *Synthesis* **2005**, 2116−2118.
(39) Geiseler, O.; Müller, M. J. *Tetrahedron* **2013**, *69*, 3683−3689.
(40) Lakowicz, J. R. *Principles of Fluorescence Spectroscopy*; Springer: New York, 2006.
(41) Apex2 Version 2.2−0 and SAINT+ Version 7.46A; Bruker Analytical X-ray System, Inc.: Madison, WI, 2007.
(42) (a) Sheldrick, G. M. SHELXTL Version 6.1; Bruker Analytical X-ray Systems, Inc.: Madison, WI, 2000. (b) Sheldrick, G. M. *Acta Crystallogr.* **2008**, *A64*, 112−122.
(43) Parr, R. G.; Yang, W. *Density-Functional Theory of Atoms and Molecules*; Oxford University Press: Oxford, 1989.
(44) Becke, A. D. *Phys. Rev. A* **1988**, *38*, 3098−3100.
(45) Lee, C.; Yang, W.; Parr, R. G. *Phys. Rev. B* **1988**, *37*, 785−789.
(46) Gaussian 09, Revision A.02: Frisch, M. J.; Trucks, G. W.; Schlegel, H. B.; Scuseria, G. E.; Robb, M. A.; Cheeseman, J. R.; Scalmani, G.; Barone, V.; Mennucci, B.; Petersson, G. A.; Nakatsuji, H.; Caricato, M.; Li, X.; Hratchian, H. P.; Izmaylov, A. F.; Bloino, J.; Zheng, G.; Sonnenberg, J. L.; Hada, M.; Ehara, M.; Toyota, K.; Fukuda, R.; Hasegawa, J.; Ishida, M.; Nakajima, T.; Honda, Y.; Kitao, O.; Nakai, H.; Vreven, T.; Montgomery, J. A., Jr.; Peralta, J. E.; Ogliaro, F.; Bearpark, M.; Heyd, J. J.; Brothers, E.; Kudin, K. N.; Staroverov, V. N.; Kobayashi, R.; Normand, J.; Raghavachari, K.; Rendell, A.; Burant, J. C.; Iyengar, S. S.; Tomasi, J.; Cossi, M.; Rega, N.; Millam, J. M.; Klene, M.; Knox, J. E.; Cross, J. B.; Bakken, V.; Adamo, C.; Jaramillo, J.; Gomperts, R.; Stratmann, R. E.; Yazyev, O.; Austin, A. J.; Cammi, R.; Pomelli, C.; Ochterski, J. W.; Martin, R. L.; Morokuma, K.; Zakrzewski, V. G.; Voth, G. A.; Salvador, P.; Dannenberg, J. J.; Dapprich, S.; Daniels, A. D.; Farkas, Ö.; Foresman, J. B.; Ortiz, J. V.; Cioslowski, J.; Fox, D. J. Gaussian, Inc.: Wallingford, CT, 2009.
(47) Tomasi, J.; Mennucci, B.; Cammi, R. *Chem. Rev.* **2005**, *105*, 2999−3093.
(48) For comparison, the energies of the excited states for the first geometry were also computed with the unrestricted functional. However, no significant differences were observed between restricted and unrestricted triplet energies, in agreement with literature precedents: Cronstrand, P.; Rinkevicius, Z.; Luo, Y.; Ågren, H. *J. Chem. Phys.* **2005**, *122*, 224104−1−10. As a result, the excited states for all geometries were computed with the restricted functional.
(49) The energy profiles for the two excited states were constructed on the basis of single-point calculations on ground-state geometries.

Although this general protocol does not take into account the relaxation of each geometry in the corresponding excited state, it is known to provide a good qualitative estimate of the course of a photochemical reaction and is computationally convenient. For examples, see: (a) Salassa, L.; Garino, C.; Salassa, G.; Gobetto, R.; Nervi, C. *J. Am. Chem. Soc.* **2008**, *130*, 9590−9597. (b) Iwamura, M.; Watanabe, H.; Ishii, K.; Takeuchi, S.; Tahara, T. *J. Am. Chem. Soc.* **2011**, *133*, 7728−7736. (c) Raymo, F. M. *J. Phys. Chem. A* **2012**, *116*, 11888−11895.

dx.doi.org/10.1021/jo5004482 | *J. Org. Chem.* 2014, 79, 3973−3981